AD-A180 050 INFRARED SKY RADIANCE DISTRIBUTIONS IN THE MARINE BOUNDARY LAYER(U) NAVAL OCEAN SYSTEMS CENTER SAN DIEGO CA W J SCHADE ET AL JAN 87 NOSC-TD-1032 1/1

UNCLASSIFIED F/G 20/6 NL

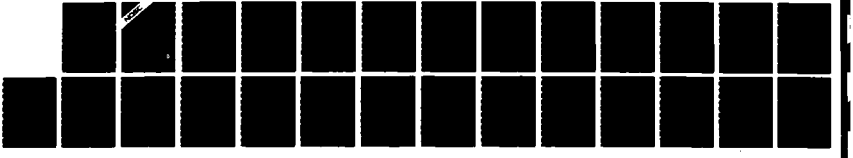

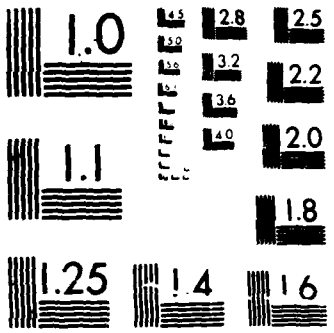

(12)

NOSC TD 1032

NOSC TD 1032

NAVAL OCEAN SYSTEMS CENTER San Diego, California 92152-5000

Technical Document 1032
January 1987

Infrared Sky Radiance Distributions in the Marine Boundary Layer

W. J. Schade
D. Law

NAVAL OCEAN SYSTEMS CENTER

San Diego, California 92152-5000

E. G. SCHWEIZER, CAPT, USN
Commander

R. M. HILLYER
Technical Director

ADMINISTRATIVE INFORMATION

This report describes the results of work funded by the Office of Naval Technology, Arlington, VA 22217. Work was completed by members of the Tropospheric Branch, Naval Ocean Systems Center, San Diego, CA 92152-5000.

Released by
H.V. Hitney, Head
Tropospheric Branch

Under authority of
J.H. Richter, Head
Ocean and Atmospheric
Sciences Division

ACKNOWLEDGEMENTS

The authors express their appreciation to H.G. Hughes and R.A. Paulus for providing radiosonde measurements. Several discussions with H.G. Hughes regarding the use of the LOWTRAN 6 computer code were especially helpful.

LH

UNCLASSIFIED
SECURITY CLASSIFICATION OF THIS PAGE

REPORT DOCUMENTATION PAGE

1a REPORT SECURITY CLASSIFICATION UNCLASSIFIED	1b RESTRICTIVE MARKINGS
2a SECURITY CLASSIFICATION AUTHORITY	3 DISTRIBUTION/AVAILABILITY OF REPORT Approved for public release; distribution is unlimited.
2b DECLASSIFICATION/DOWNGRADING SCHEDULE	
4 PERFORMING ORGANIZATION REPORT NUMBER(S) NOSC TD 1032	5 MONITORING ORGANIZATION REPORT NUMBER(S)
6a NAME OF PERFORMING ORGANIZATION Naval Ocean Systems Center 6b OFFICE SYMBOL (If applicable) Code 543	7a NAME OF MONITORING ORGANIZATION
6c ADDRESS (City, State and ZIP Code) San Diego, CA 92152-5000	7b ADDRESS (City, State and ZIP Code)
8a NAME OF FUNDING/SPONSORING ORGANIZATION Office of Naval Technology 8b OFFICE SYMBOL (If applicable)	9 PROCUREMENT INSTRUMENT IDENTIFICATION NUMBER
8c ADDRESS (City, State and ZIP Code) Arlington, VA 22217	10 SOURCE OF FUNDING NUMBERS PROGRAM ELEMENT NO: 62759N PROJECT NO: W59551 TASK NO: RW59551B AGENCY ACCESSION NO: DN888 715

11 TITLE (Include Security Classification)
Infrared Sky Radiance Distributions in the Marine Boundary Layer

12 PERSONAL AUTHOR(S)
W.J. Schade and D. Law

13a TYPE OF REPORT	13b TIME COVERED	14 DATE OF REPORT (Year, Month, Day)	15 PAGE COUNT
Interim	FROM _____ TO _____	January 1987	26

16 SUPPLEMENTARY NOTATION

17 COSATI CODES			18 SUBJECT TERMS (Continue on reverse if necessary and identify by block number)
FIELD	GROUP	SUB-GROUP	Infrared sky radiance distributions Atmospheric transmittance aerosols

19 ABSTRACT (Continue on reverse if necessary and identify by block number)

This report describes an alternative method for inferring the effects of aerosols on atmospheric transmittance. Spatial distributions of infrared sky radiance in the 3 to 5 μm (SWIR) and 8 to 12 μm (LWIR) spectral bands were measured at low elevation angles above the sea surface, then compared with the corresponding clear-sky radiance. The infrared aerosol transmittance was inferred from the ratio of measured radiance to calculated clear-sky radiance along the horizon line of sight (LOS). Results show that only the LWIR band can be used to infer aerosol transmittance reliably. The radiance along the horizon LOS originates predominately in the lowest 100 m of the atmosphere; therefore, reasonably accurate horizon radiance of transmittance predictions could be made from meteorological data within this low altitude.

20 DISTRIBUTION/AVAILABILITY OF ABSTRACT	21 ABSTRACT SECURITY CLASSIFICATION	
☐ UNCLASSIFIED/UNLIMITED ☒ SAME AS RPT ☐ DTIC USERS	UNCLASSIFIED	
22a NAME OF RESPONSIBLE INDIVIDUAL D. Law	22b TELEPHONE (Include Area Code) (619) 225-7200	22c OFFICE SYMBOL Code 754

DD FORM 1473, 84 JAN

83 APR EDITION MAY BE USED UNTIL EXHAUSTED
ALL OTHER EDITIONS ARE OBSOLETE

UNCLASSIFIED
SECURITY CLASSIFICATION OF THIS PAGE

DD FORM 1473, 84 JAN

CONTENTS

ILLUSTRATIONS

TABLES

INTRODUCTION

The effects of aerosols on the propagation of infrared radiation through the marine boundary layer are basic in the use of both active and passive remote sensing systems over the ocean. The extent to which these effects can be evaluated and modeled depends largely on the methods for characterizing the atmospheric constituents along the optical path.

Current methods for measuring particle sizes and concentrations are limited to local sampling volumes at the sensor site which are not characteristic of extended path lengths. Lidar measurements have been used to compute total volume extinction coefficients as a function of range (Hughes et al., 1981); however, lidar data are generally acquired at sequential intervals along different directions between which the meteorological conditions could change without notice. Additional uncertainties arise when lidar data at one wavelength are applied to other spectral regions.

An alternative method for inferring the effects of aerosols on atmospheric transmittance is described in this report. Spatial distributions of infrared sky radiance in the 3- to 5-μm short wavelength infrared (SWIR) and 8- to 12-μm long wavelength infrared (LWIR) spectral bands were measured at low elevation angles above the sea surface. These distributions represent the integrated radiance propagated along contiguous optical paths through the entire atmosphere within the field of view (FOV) of a calibrated thermal imaging sensor. Since the FOV of this AGA Thermovision 780 is scanned in 40 ms, the data for each distribution are almost simultaneous.

The extent to which the measured radiance differs from the corresponding clear-sky radiance can be used to imply the effective transmittance. The clear-sky radiance was computed with the LOWTRAN 6 computer code (Kneizys et al., 1983) using radiosonde measurements of meteorological parameters concurrent with the measured radiance over the ocean. This technique offers a viable method for evaluating the total aerosol effect through the entire marine boundary layer by remote sensing. At present, the database for this technique is limited to almost-clear-sky conditions along the horizon line of sight (LOS).

The data were obtained during one diurnal cycle starting 15 April 1986 at 1500 Pacific Standard Time (PST) and ending 16 April 1986 at 1730 PST. The sensor LOS was directed along an azimuth of 270 degrees true radial from NOSC, building T323, located at 32.699 degrees N latitude, 117.253 degrees W longitude, at a height of 33 m above sea level.

Radiosondes were released from the deck ot the USS POINT LOMA (AGDS 2) about 7.6 m above the sea surface at a range of 5 km from the sensor site. Wind speed, direction, and sea temperatures were also recorded on board the ship, as well as cloud conditions. A complete description of the shipboard data is available (Jensen, 1986).

Throughout this report, clear-sky radiance refers to the atmosphere without aerosols. This corresponds to IHAZE = O in the LOWTRAN 6 computer code when ts = 1 in the LOWTRAN calculations for sky radiance (where ts is transmittance due to scattering). This is regarded as the reference condition for comparing the respective measurements in the LWIR and SWIR spectral bands.

ATMOSPHERIC MEASUREMENTS

Infrared sky radiance and meteorological measurements were recorded simultaneously in a series of four data sets. Table 1 lists the dates and times for the

measurements along with the solar positions. Surface meteorological measurements were made at the NOSC sensor site as well as shipboard, while the vertical profiles were measured by radiosondes (radiosonde observation) released from the USS POINT LOMA. The air and sea temperatures, wind speed, and direction are also listed in table 1.

Table 1. Atmospheric measurements series for meteorological parameters.

Data Set	1	2	3	4
Date	15 Apr 86	16 Apr 86	16 Apr 86	16 Apr 86
Radiosonde Time (PST)	1945	0845	1245	1645
Solar Position (degrees)				
Azimuth	295	106	212	270
Zenith	140	49	26	71
Air Temp. (°C)	15.0	15.4	15.5	15.7
Wind Speed (knots)	10	9	20	20
Direction (degrees)	300	330	280	310
Sea Temp. (°C)	17.8	16.7	17.2	17.2

Figures 1, 2, 3, and 4 show the radiosonde measurements for temperature and relative humidity plotted with respect to altitude. These data were used in the LOWTRAN 6 computer code to calculate clear-sky radiance as a function of elevation angle above the horizon. The data in figure 1 were used to evaluate the meteorological sensitivities of the radiance calculations. This set presents the nighttime data for a well-defined cloud-top boundary and an adiabatic lapse rate of 9.8°C in the first kilometer above sea level.

The uncertainty in relative humidity is estimated to be 5 percent, which provides a better approximation to the water vapor density than any of the standard model atmospheres. The sensitivity of the radiance calculations to this uncertainty in humidity was examined by incrementing the relative humidity profile ±5 percent while keeping the temperature profile unchanged from the measured values. Similarly, the sensitivity to the temperature uncertainty of ±0.5°C was evaluated for the observed relative humidity profile of figure 1.

Figure 5 shows the comparative effects of deviations in temperature and relative humidity. The calculated clear-sky radiance, for IHAZE = O, is plotted as a function of elevation angle. Radiance discrepancies resulting from relative humidity errors are less than those resulting from temperature errors throughout the range of elevation from 0 to 2 degrees. For elevation less than 0.5 degree, the effects of errors in relative humidity are negligible compared with those in temperature. A temperature error of ± 0.5°C changes the radiance by about ±0.033 mw/(cm^2 - str) in the LWIR band and about ±0.0033 mw/(cm^2 - str) in the SWIR band.

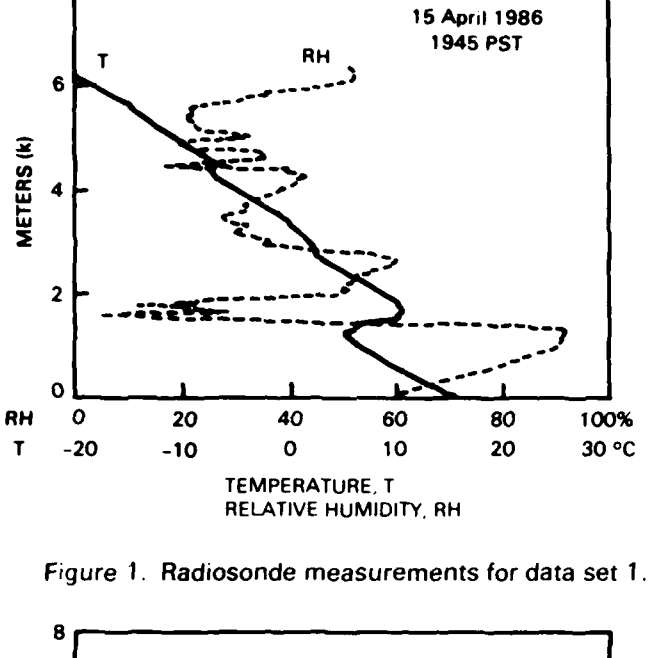

Figure 1. Radiosonde measurements for data set 1.

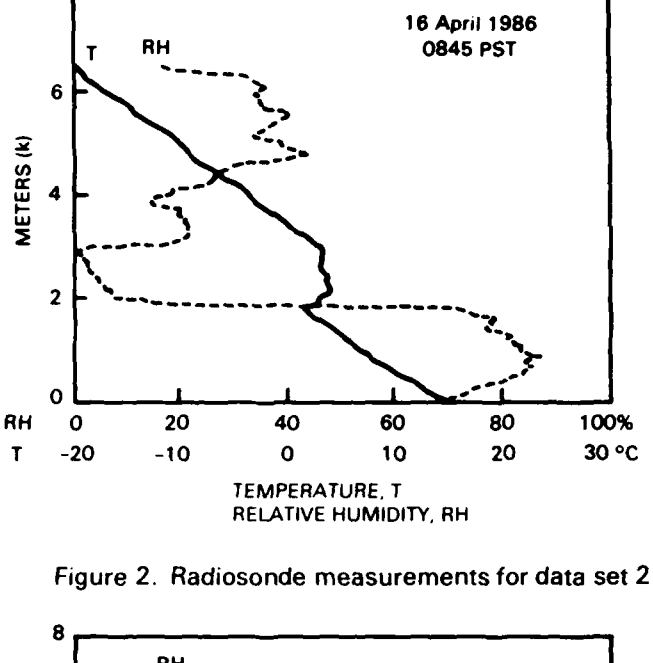

Figure 2. Radiosonde measurements for data set 2.

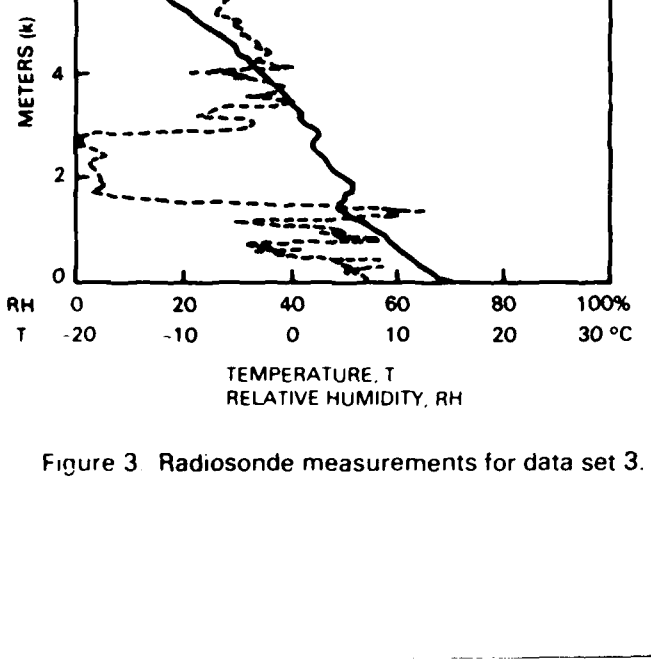

Figure 3 Radiosonde measurements for data set 3.

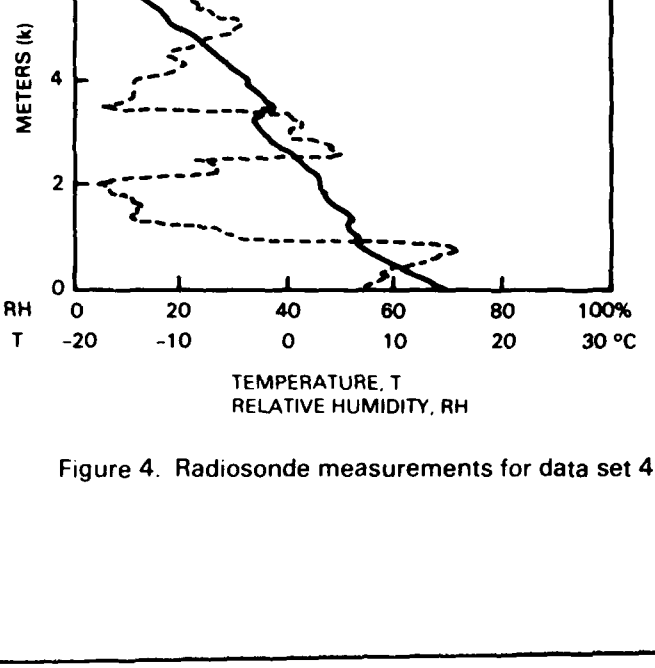

Figure 4. Radiosonde measurements for data set 4.

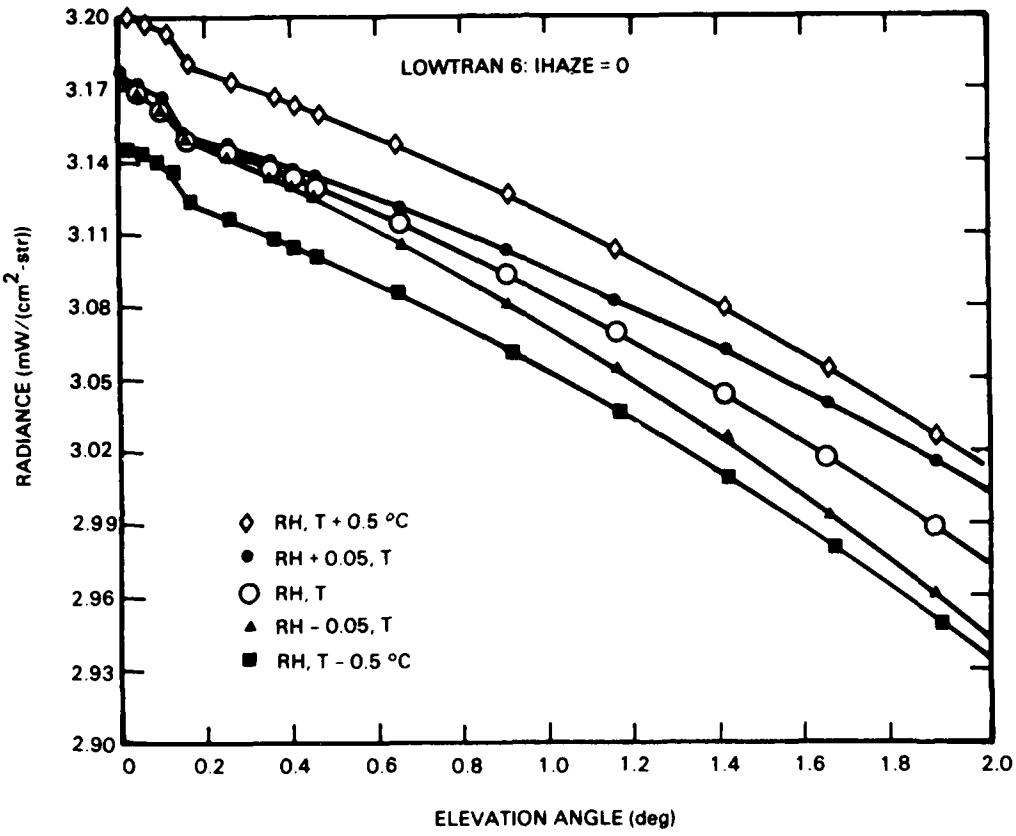

Figure 5. Calculated clear-sky distributions of LWIR radiance above the horizon for comparative errors in temperature (T ± 0.5°C) and relative humidity (RH ± .05) profiles.

Sky radiance data were acquired in the 3.5- to 5.5-μm and 8- to 12-μm spectral bands simultaneously with the AGA 780 dual scanning systems functioning as imaging radiometers. The operational characteristics of the sensor systems are listed in table A1 of the appendix. Figure A1.a shows the main components of each system. The analog video signals in the 3- by 3-degree FOV are interfaced through a Datalink analog-to-digital converter to a digital image processor. The format of the digital display is 128 by 128 pixels with 8-bit resolution. The minimum detectable temperature difference (MDTD) between adjacent infrared fields of view (IFOVs) is 0.1°C.

The total system response for each spectral band is calibrated in isotherms which represent the video signal amplitudes for radiation from a blackbody at a measured temperature and close range. Sets of conversion curves relating isotherms to object temperatures (with emissivity = 1) are obtained with the expression

$$I = C1/(C3 \cdot \exp(C2/T) - 1), \quad (1)$$

where T is the blackbody temperature in degrees Kelvin. The constants C1, C2, and C3 are derived for the calibration source at several different temperatures. Figure A1.b shows a sample set of curves.

The original image is analyzed with the microcomputer by assigning the equivalent blackbody temperature to the corresponding isotherm value for selected pixels in the FOV, through the transposition of equation 1,

$$T = C2/\ln u, \tag{2}$$

where

$$u = ((C1/I) + 1)/C3.$$

Radiance values are computed for each blackbody temperature through the integration of Planck's equation for the appropriate spectral band. The final form of the equation for radiance as a function of isotherms is

$$L(SB,T) = a \cdot I(T) - b, \tag{3}$$

where SB is the spectral band, a is the slope, b is the intercept, and I(T) is a nonlinear function of T in equation 1. The constants for converting isotherms to radiance in equation 3 are listed in table A2 for each spectral band, as well as the calibration source characteristics.

The main source of uncertainty in the conversion to radiance is in the isotherm values for the video signal amplitudes. Isotherms are calculated with the microcomputer to within ±0.1, so that the temperature of the calibration source is reproduced within ±0.2°C. This uncertainty in the temperature causes a radiance error of ±0.01 mw/(cm^2 - str) in the LWIR band, and ±0.001 mw/(cm^2 - str) in the SWIR band. Details of the error analysis are presented in the appendix.

In each of the four data sets, both infrared sensor systems were referenced to a calibration source at ambient air temperature within 1 hour prior to the radiosonde ascent. Thermal images of sky radiance were recorded continuously on analog video tape and sequentially on digital diskette during 1 hour preceding and following the radiosonde measurements. These data provide an unambiguous verification of either the stability or variability of the sky radiance distributions during meteorological measurements. No measurable changes were observed during each of the data sets reported here, except for temporal variations in cloudiness.

RADIANCE DISTRIBUTIONS

Figure 6 shows the four LWIR radiance distributions as a function of elevation angle above the optical horizon. Zero degrees elevation corresponds to the IFOV tangent to the sea surface where the radiance is maximum. The elevation IFOV angular subtense of 0.05 degree is shown in the figure as well as the radiance uncertainty corresponding to a temperature deviatior of TD = ±0.2°C.

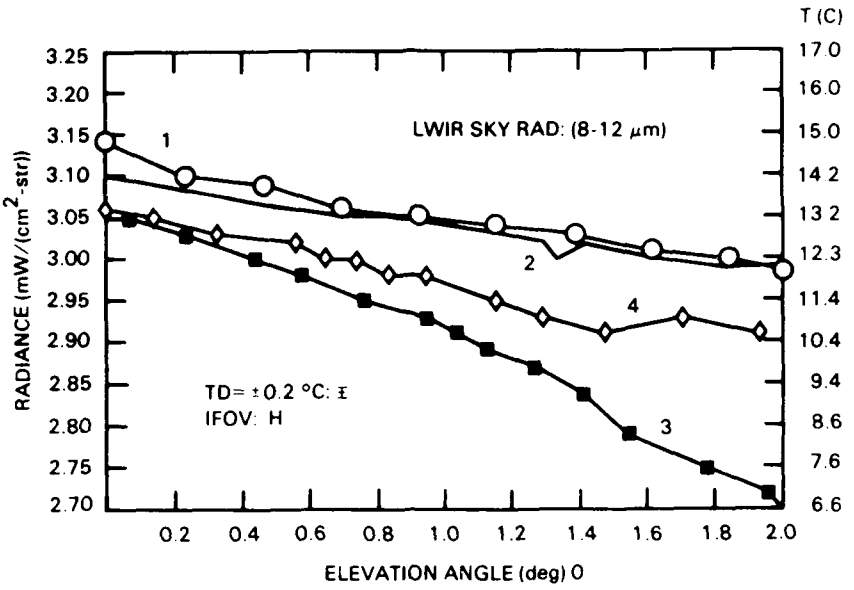

Figure 6. LWIR sky radiance distributions above the horizon; plot 1: 15 April 86, 1945 PST; plot 2: 16 April 86, 0845 PST; plot 3: 16 April 86, 1245 PST; plot 4: 16 April 86, 1645 PST.

Cloud radiance contributions are apparent at elevations greater than 0.4 degree. Scattered solar radiation from clouds is especially notable in data set 4, when the sun is about 20 degrees above the sensor LOS.

The radiances for data sets 3 and 4 are equal within the measurement uncertainty, for low elevations between 0 and 0.3 degree; however, the solar zenith angle changed from 26 degrees in data set 3 to 71 degrees in data set 4. These conditions imply that aerosol scattering of solar radiation is negligible in the LWIR band since the meteorological parameters are nearly the same for these two data sets as shown in figures 3 and 4.

Figure 7 shows the SWIR sky radiance distributions. These four plots are concurrent with those of the LWIR data. On the radiance scale used in figure 7, plots 1, 2, and 3 are approximately equal, within the temperature deviation TD = ±0.2°C. Plot number 4 shows a very large increase in radiance resulting from scattered solar radiation in the clouds and lower atmospheric levels. The high effective temperature of this background scattering provides large target-to-background contrasts in the SWIR band for objects near ambient air temperature. The equivalent blackbody temperature scales are shown along the ordinates on the right of figures 6 and 7.

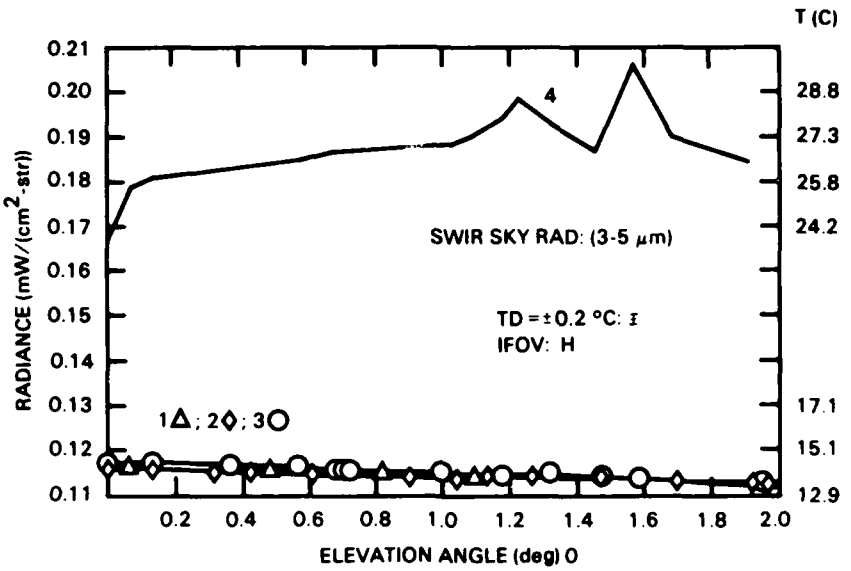

Figure 7. SWIR sky radiance distributions above the horizon and coincident with the LWIR distributions.

Figures 8 and 9 compare the observed radiance distributions and the corresponding calculated clear-sky radiances. Figures 8a, b, c, and d show the distributions for the LWIR band, and figures 9a, b, c, and d show those for the SWIR band.

The clear-sky radiances were calculated using atmospheric models with 30 layers in the LOWTRAN 6 computer code. The meteorological entries were provided by the radiosonde data which are tabulated in table A3 in the appendix. The concentrations of uniformly mixed gases and ozone were those in the 1962 U.S. Standard model atmosphere.

The importance of the humidity and temperature lapse rates in calculating sky radiance distributions in the boundary layer was noted previously (Ben-Shalom, Devir, and Lipson, 1983). Accordingly, the first kilometer above sea level was divided into 10 levels with about 1°C increments for each 100 m between levels. The remaining atmosphere was divided into 20 levels between 1 and 5.5 km. The radiosonde data terminated at about 6 km.

The LOWTRAN expression for calculating atmospheric radiance (Kneizys et al., 1980) is

$$L(SB) = \sum_{i=1}^{N-1} (\underline{ta}(i) - \underline{ta}(i+1))B\left(SB, \frac{T(i)+T(i+1)}{2}\right)\left(\frac{\underline{ts}(i)+\underline{ts}(i+1)}{2}\right)$$

$$+ B(SB,T(b))\underline{tb}, \qquad (4)$$

where the summation along a specified LOS is over (N - 1) isothermal layers at temperatures T(i), and

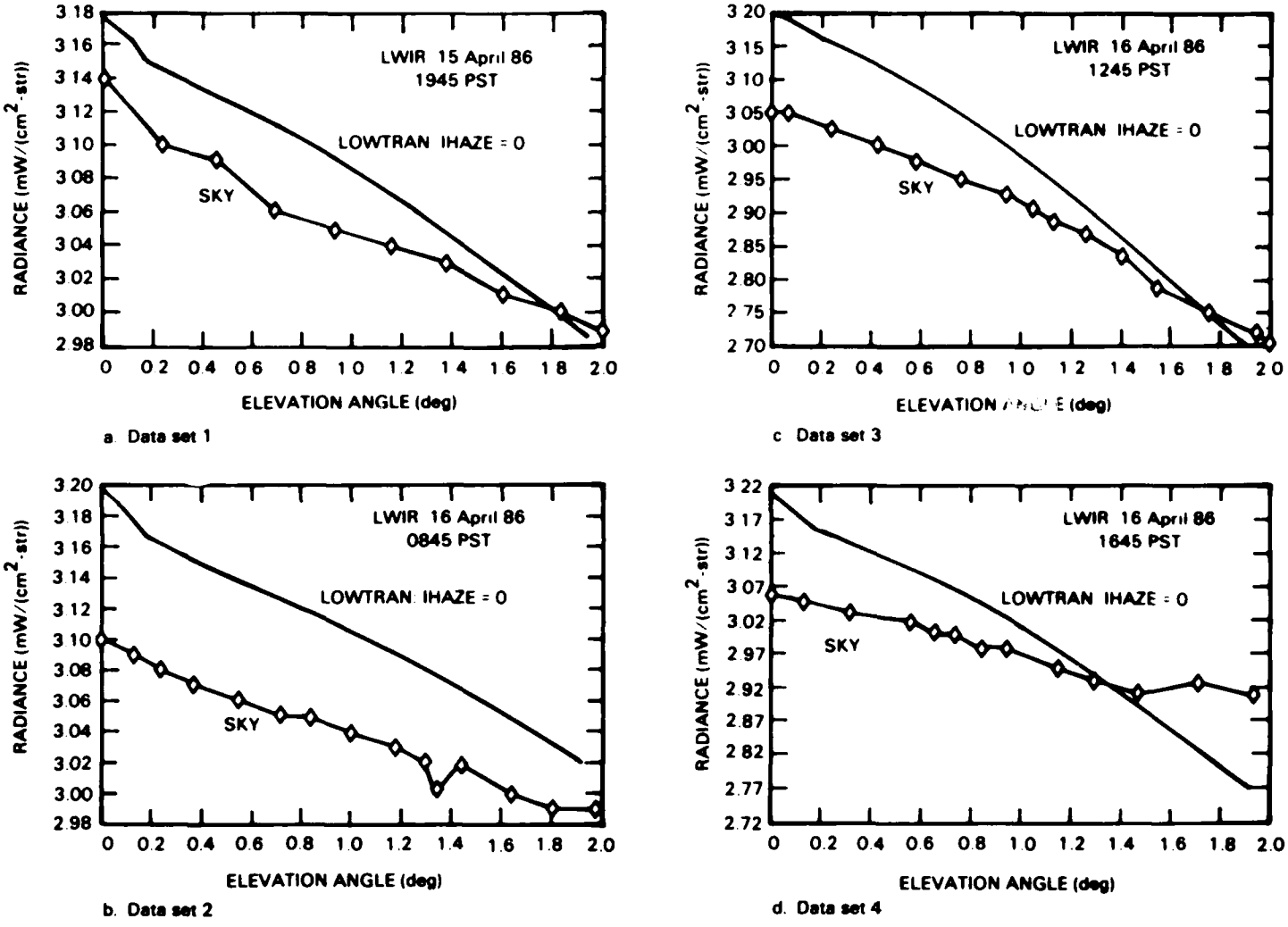

Figure 8. Comparison of measured LWIR sky radiance distributions with calculated clear-sky radiance from LOWTRAN 6: IHAZE = 0.

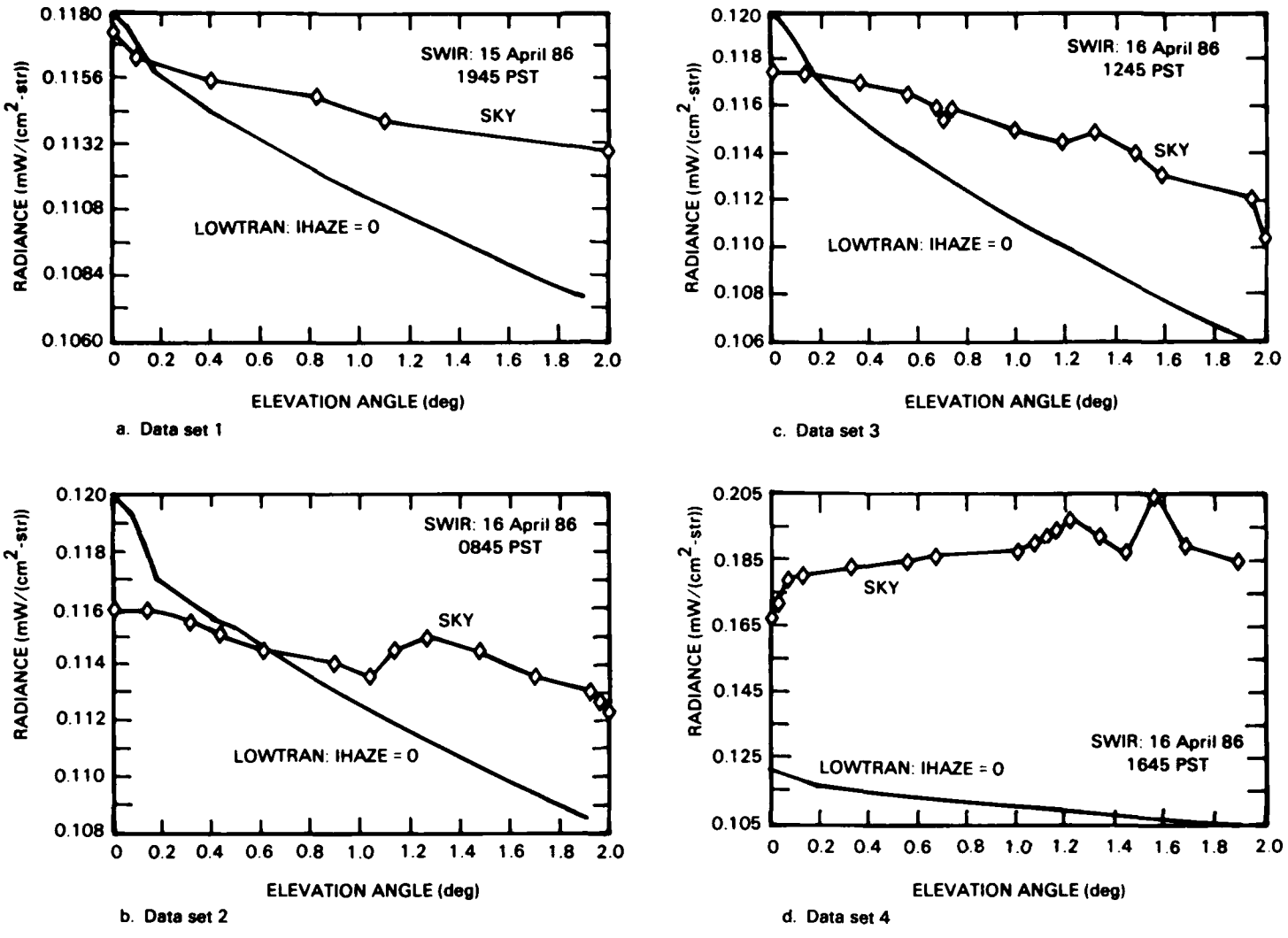

Figure 9. Comparison of measured SWIR sky radiance distributions with calculated clear-sky radiance from LOWTRAN 6: IHAZE = 0.

SB = spectral band: 3 to 5 μm or 8 to 12 μm

ta = band average transmittance due to absorption,

ts = band average transmittance due to single scattering,

tb = band average transmittance from sensor to cloud boundary,

B(SB,T) = Planck blackbody function for a spectral band and average temperature T of an atmospheric layer.

To avoid the effects of cloud radiance, the comparison of observed-to-calculated radiance is restricted to the horizon LOS where the atmospheric optical depth and aerosol attenuation are greatest. Along zero elevation, the LWIR molecular (absorption) transmittance, ta, is less than 1×10^{-4} through the 137-km horizontal optical path to the cloud base. With a cloud-base temperature of 6.8°C, the maximum LWIR cloud radiance is 2.7 mw/(cm^2 - str), which becomes negligible at the sensor aperture.

For calculation of clear-sky radiance, ts = 1 for all atmospheric layers. Along the horizon LOS, the sky radiance originates predominantly in the lowest layer which approximates a horizontally homogeneous atmosphere about 100 m high. This condition is clearly evident in table 2 which lists the LWIR radiance and band average absorption transmittance, ta, for ranges along the horizon LOS to five levels in the first nine atmospheric layers. Over 99 percent of the clear-sky radiance along the horizon LOS is attributable to the lowest 100 m of the atmosphere. Within this lowest layer, equation 4 reduces to

$$L(SB,1) = (1 - ta(1))\, B(SB,T(1)). \quad (5)$$

From table 2, $ta(1) \simeq .004$, so the emissivity of the lowest layer, $e(1) = 1 - ta(1)$, is very close to unity through application of Kirchoff's law. Thus, the clear-sky radiance in the lowest layer should equal the blackbody radiance at ambient air temperature as reported previously (Bennett et al., 1960; Bell et al., 1960). The effects of aerosols on infrared sky radiance can be inferred from equations 4 and 5 by including the transmittance due to scattering. The transmitted radiance along the horizon LOS then becomes

$$L(SB)' = L(SB) \cdot ts, \quad (6)$$

where L(SB) is the clear-sky radiance given by equation 5 extended to all 30 layers.

Table 2. LWIR radiance and transmittance along the horizon LOS for data set 1, LOWTRAN 6 : IHAZE = 0.

Layers	Altitude to top (m)	Range to top (km)	Radiance mw/(cm^2 - str)	%Max Radiance	Average Transmittance
1	143	67	3.163	99.7	0.0036
2	263	84	3.171	99.9	0.0011
3	383	97	3.172	99.9	0.0004
5	575	114	3.173	100	0.0001
9	1016	145	3.173	100	0.0000

Absorption by aerosols would tend to bring the emissivity of the atmosphere closer to unity through ta, which would change by less than 1 percent from the transmittance due to molecular absorption for clear-sky conditions. Molecular scattering, however, is negligible in the spectral range of 3 to 12 μm, so ts can be assigned primarily to aerosols. Thus, the scattering transmittance, ts, was calculated with equation 6 using the measured sky radiance for L(SB)', which represents the transmitted radiance along the optical LOS from the sensor receiving aperture to space.

A summary of the horizon sky temperatures and aerosol transmittance is presented in table 3 for each set of radiosonde data. The temperatures corresponding to the measured horizon sky radiance and calculated clear-sky radiance are listed for the LWIR and SWIR bands. The radiosonde base temperatures and sensor (local) air temperatures are also given. Within each data set, the temperature differences are less than the uncertainties in the measurements except for the equivalent temperatures of the measured sky radiances. Reduced equivalent temperatures in the LWIR band correspond to aerosol scattering loss in radiance, while the increased temperature in the SWIR indicates additional radiance from scattered solar radiation in data set 4.

The calculated aerosol transmittances for both infrared bands are listed in table 3. The LWIR values show a slight aerosol effect in data sets 3 and 4, but the SWIR values are inconsistent. Although the values for both infrared bands agree in the nighttime and morning runs when the aerosols were negligible, the SWIR band cannot be used reliably to indicate aerosol attenuation when scattered solar radiation must be included. As noted above, the horizon LWIR values were unaffected by solar scattering for zenith angles from 26 to 71 degrees.

Table 3. Horizon sky temperature and aerosol transmittance.

Data Set	1	2	3	4
Date	15 Apr 86	16 Apr 86	16 Apr 86	16 Apr 86
Time (PST)	1945	0845	1245	1645
RAOB Base (±0.5°C)	15.0	15.4	15.5	15.7
Local Air (±0.3°C)	14.6	15.2	15.1	15.8
LOWTRAN 6: Clear-Sky				
SWIR	14.6	15.1	15.1	15.2
LWIR	15.4	15.9	15.9	16.1
Measured Sky (±0.2°C)				
SWIR	14.5	14.2	14.5	23.7
LWIR	14.7	14.2	13.1	13.4
Aerosol Transmittance				
SWIR	.99	.97	.98	1.38
LWIR	.99	.97	.95	.95

CONCLUSIONS

The AGA Thermovision 780 dual scanning system was used to measure infrared sky radiance distributions in the SWIR and LWIR spectral bands simultaneously. Sequential images of radiance distributions provided control data for monitoring the stability or variability of atmospheric conditions throughout the concurrent time for radiosonde ascent.

Measured infrared sky radiance distributions were compared with the corresponding clear-sky radiance using the LOWTRAN 6 computer code. The presence of cloud radiance and scattered solar radiation restricted the comparison to elevations close to the horizon where aerosol attenuation would be greatest.

The infrared aerosol transmittance was inferred from the ratio of measured radiance to calculated clear-sky radiance along the horizon LOS. The equivalent temperatures for blackbody radiance at the horizon were either less than or equal to the ambient air temperature near the sea surface, except when the SWIR band included scattered solar radiation. The inclusion of scattered solar radiation in the SWIR band yields a high contrast background for targets near ambient air temperature. Because of this, only the LWIR band can be used to infer aerosol transmittance reliably.

The radiance along the horizon LOS originates predominantly in the lowest 100 m of the atmosphere; therefore, reasonably accurate horizon radiance or transmittance predictions could be made from meteorological data within this low altitude. These conclusions suggest that a LWIR aerosol transmissometer could be developed by computing the ratio of the measured horizon sky radiance to the calculated clear-sky radiance using the local ambient meteorological data. Such a point-measuring system would only require a calibrated nonimaging radiometer to record the radiance along the horizon LOS.

The meager database for these conclusions denotes the need for additional measurements and analysis. The data presented herein corresponds to almost-clear-sky conditions. Infrared sky radiance distributions should be measured for a large variety of atmospheric conditions to evaluate the range of correlations with meteorological parameters at the sensor site.

REFERENCES

Bell, E.E., L. Eisner, J. Young, and R.A. Oetjen (1960). Spectral Radiance of Sky and Terrain at Wavelengths between 1 and 20 Microns. II. Sky Measurements, J. Opt. Soc. Am. 50(12):1313-1320.

Bennett, H.E., J.M. Bennett, and M.R. Nagel (1960). Distribution of Infrared Radiance over a Clear-Sky, J. Opt. Soc. Am. 50(2):100-106.

Ben-Shalom, A., A.D. Devir, and S.G. Lipson (1983). Opt. Eng. 22:460.

Hughes, H.G., D.R. Jenson, D.H. Stephens, and J. Lentz (1981). A Modified Gamma Aerosol Model Beneath Maritime Stratus Based On Lidar Return, Naval Ocean Systems Center TN 1079*.

Jensen, D.R. (1986). Temperature Measurements of the USS Point Loma for FLIR Evaluation Studies, Naval Ocean Systems Center TD 971.

Kneizys, F.X., E.P. Shettle, W.O. Gallery, J.H. Chetwynd, Jr., L.W. Abreu, J.E.A. Selby, R.W. Fenn, and R.A. McClatchey (1980). Atmospheric Transmittance/ Radiance: Computer Code LOWTRAN 5, Air Force Geophysics Laboratory AFGL-TR-80-0067.

Kneizys, F.X., E.P. Shettle, W.O. Gallery, J.H. Chetwynd, Jr., L.W. Abreu, J.E.A. Selby, R.W. Fenn, and R.A. McClatchey (1983). Atmospheric Transmittance/ Radiance: Computer Code LOWTRAN 6, Air Force Geophysics Laboratory AFGL-TR-83-0187.

*Technical notes (TNs) are working documents and do not represent an official policy statement of the Naval Ocean Systems Center. For further information, contact the author.

APPENDIX

ERROR ANALYSIS FOR CONVERSION OF ISOTHERMS TO RADIANCE

Table A1 shows the relevant system parameters for the AGA Thermovision 780 dual scanning imaging radiometer. Figure A1.a shows a block diagram of the AGA Thermovision 780 imaging system as a whole. Figure A1.b shows typical conversion curves for isotherm units to temperature.

From equation 3 in the text, an incremental change in radiance resulting from an incremental change in temperature is given by

$$DL/DT = a \frac{(C1 \cdot C2 \cdot C3 \cdot \exp(C2/T)}{(T(C3 \cdot \exp(C2/T) - 1))^2} \text{ (mw/(cm}^2 \text{ - str °K))}. \qquad \text{(A1)}$$

Equation A1 was evaluated with an HP-85 microcomputer by substituting the appropriate constants from table A2. The results are shown in figure A2.a for the SWIR band and figure A2.b for the LWIR band as functions of temperature in degrees centigrade. In both cases, the incremental temperature is DT = 1°K.

Table A3 shows the radiosonde measurements that were used in the LOW 6 calculations and correspond to the plots shown in text figures 1 through 4.

Table A1. AGA Thermovision 780 dual scanning systems operational characteristics.

Scanner	SWIR	LWIR	BOTH
Spectral Band: μm	3.5 to 5.5	8 to 12	
Detector: 1 each	InSb	HgCdTe	
Temperature: °K			77
FOV (az by el): degrees			3 by 3
IFOV (az by el): mrad			1.2 by 0.9
Telescope Objective			
Diameter: cm			10.6
Focal Ratio			1.8
FOV Scan Mode			
Horiz. Line Time: ms			0.4
Vert. Field Time: ms			40
Field Rate: Hz			25
Frame Rate: Hz			6.25
IFOV dwell: μs			5.3
Signal Processing: AC + DC Restored			
MDTD: °C/IFOV			0.1
Temp. Range: °C			-20 to 1000

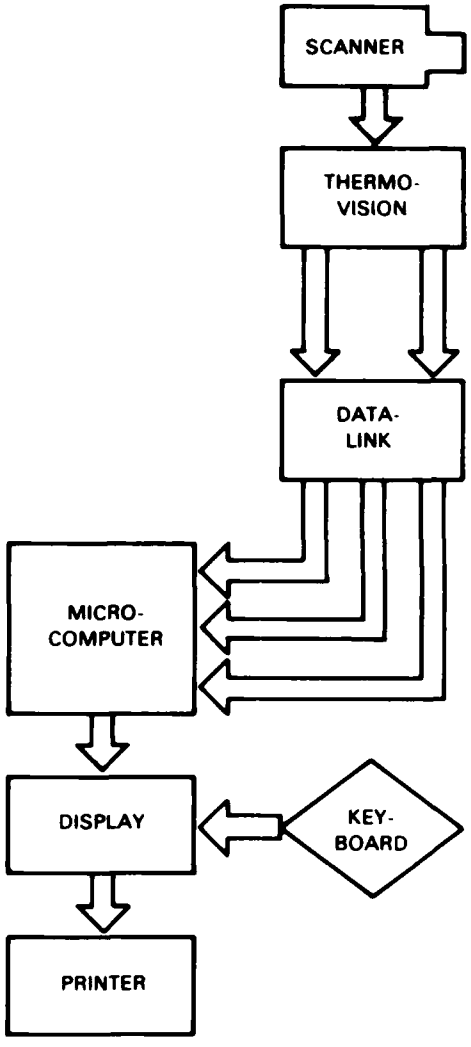

Figure A1.a. Schematic diagram of the AGA Thermovision 780 imaging system.

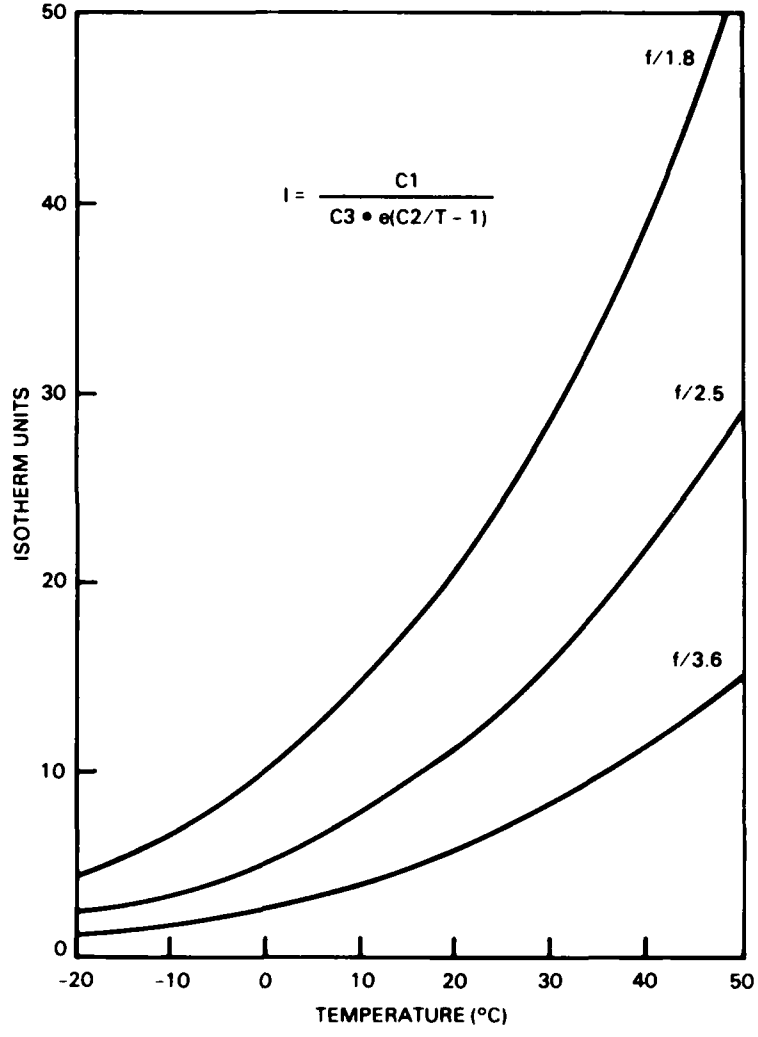

Figure A1.b. Typical curves for converting isotherms to temperature of the source.

Table A2. Calibration constants for converting isotherms to radiance.

Scanner	SWIR	LWIR	BOTH
C1: isotherms	383140.4	1514.4	
C2: °K	2945.0	1294.2	
C3: dimensionless	1.0	0.503	
a: mw/(cm^2 - str- isotherm)	$9.695 \cdot 10^{-6}$	$1.002 \cdot 10^{-4}$	
b: mw/(cm^2 - str)	$1.556 \cdot 10^{-5}$	$1.002 \cdot 10^{-4}$	
Calibration Source			
Distance: m			3.0
Emissivity: ±0.01			0.98
Temperature: ±0.1°C			15-100

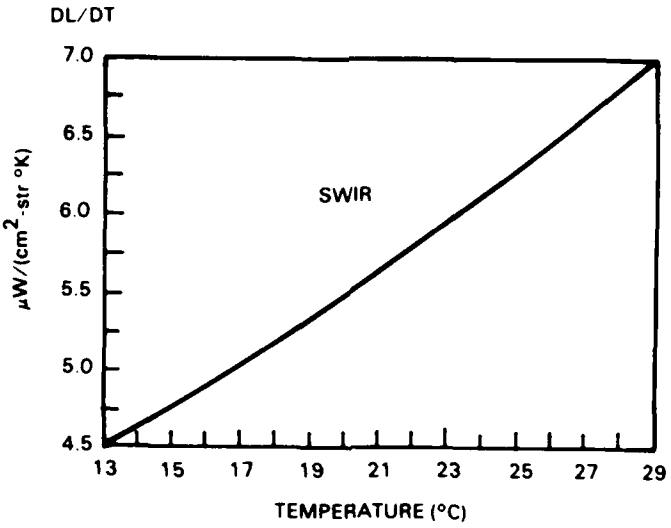

Figure A2.a. Incremental change in SWIR radiance for an incremental change in temperature of 1°K.

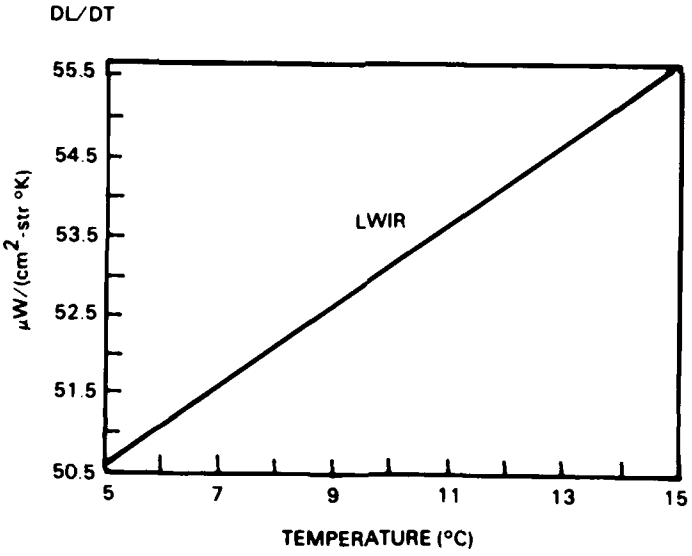

Figure A2.b. Incremental change in LWIR radiance for an incremental change in temperature of 1°K.

TABLE A3. Radiosonde measurements
USS POINT LOMA (AGDS-2)

15 April 1986
1945 PST

Z (KM)	P (MB)	T (K)	REL H (%)
.008	1015.800	288.05	60.00
.143	999.700	287.05	64.00
.263	985.500	285.75	68.00
.383	971.600	284.55	72.00
.501	957.800	283.25	75.00
.575	949.300	282.65	78.00
.738	930.900	281.25	84.00
.870	916.100	280.15	87.00
.901	912.900	279.95	89.00
1.016	900.000	279.15	91.00
1.238	876.200	278.35	91.00
1.369	862.300	279.15	51.00
1.560	842.600	283.45	5.00
1.648	833.600	283.45	25.00
1.767	821.800	283.25	15.00
1.988	800.200	281.65	49.00
2.296	770.800	278.85	52.00
2.514	750.500	276.95	58.00
2.644	738.600	275.95	59.00
2.759	728.100	275.35	55.00
2.932	712.700	274.85	35.00
3.075	700.100	274.15	32.00
3.503	663.700	272.15	29.00
4.247	604.000	265.75	41.00
4.344	596.300	265.45	39.00
4.455	588.000	265.75	18.00
4.565	579.700	265.55	34.00
4.676	571.500	264.45	34.00
4.841	559.400	263.25	20.00
5.006	547.600	262.15	31.00
5.101	540.800	261.45	23.00
5.535	510.900	258.45	21.00
5.697	500.100	257.45	29.00

16 April 1986
0845 PST

Z (KM)	P (MB)	T (K)	REL H (%)
.009	1014.800	288.55	65.00
.068	1007.600	287.55	70.00
.143	998.700	286.85	73.00
.218	989.800	286.25	75.00
.308	979.300	285.45	78.00
.428	965.400	284.45	81.00
.532	953.500	283.45	84.00
.650	940.000	282.45	86.00
.783	925.100	281.45	86.00
.843	918.500	280.95	86.00
.901	912.000	280.75	86.00
1.018	899.100	280.15	84.00
1.123	889.500	279.45	83.00
1.225	978.500	278.75	81.00
1.356	864.500	277.95	80.00
1.458	853.900	277.15	78.00
1.544	844.800	276.45	78.00
1.629	834.300	275.85	78.00
1.773	819.600	274.95	72.00
1.903	806.500	276.15	15.00
2.047	792.300	277.35	8.00
2.957	708.200	276.65	2.00
3.087	697.000	275.45	20.00
3.658	649.100	271.85	21.00
3.899	629.700	270.25	16.00
4.292	599.100	268.05	25.00
4.612	575.000	265.05	33.00
4.778	562.900	264.25	43.00
5.149	536.500	262.75	35.00
5.531	510.400	259.45	40.00

16 April 1986
1245 PST

Z (KM)	P (MB)	T (K)	REL H (%)
.008	1017.700	288.65	50.00
.083	1008.700	287.55	54.00
.158	999.700	286.75	54.00
.233	990.900	286.25	52.00
.264	987.400	286.05	54.00
.338	978.600	285.25	50.00
.457	964.800	284.35	49.00
.590	949.400	283.35	35.00
.650	942.700	283.25	31.00
.724	934.300	282.75	36.00
.798	926.100	282.45	57.00
.856	911.500	282.05	49.00
.931	911.300	281.75	48.00
.960	908.100	281.55	49.00
1.034	900.000	280.75	48.00
1.122	890.500	280.25	32.00
1.384	862.400	278.15	63.00
1.515	848.700	277.75	23.00
1.689	830.700	278.45	4.00
2.412	760.000	275.95	5.00
2.700	733.400	275.15	1.00
2.843	720.400	275.65	4.00
2.930	712.800	274.95	32.00
3.102	697.700	273.85	32.00
3.159	692.800	273.95	24.00
3.330	678.100	273.35	26.00
3.459	667.300	272.85	39.00
3.729	645.100	271.45	37.00
4.040	620.400	270.05	26.00
4.152	611.600	269.35	36.00
5.085	542.800	264.05	27.00
5.687	501.900	260.25	28.00

16 April 1986
1645 PST

Z (KM)	P (MB)	T (K)	REL H (%)
.008	1016.100	288.85	50.00
.083	1007.100	287.25	54.00
.143	999.900	286.55	56.00
.233	989.300	285.75	58.00
.308	980.600	285.25	58.00
.413	968.400	284.25	60.00
.427	966.700	284.05	58.00
.575	949.600	282.55	66.00
.722	932.900	281.25	71.00
.738	931.200	281.05	71.00
.869	916.400	279.95	71.00
.895	914.800	279.75	71.00
.957	906.700	279.45	54.00
.987	903.400	279.75	31.00
1.015	900.200	279.75	30.00
1.177	882.800	278.95	28.00
1.323	867.200	279.25	13.00
1.483	850.400	279.15	11.00
1.860	811.900	276.75	9.00
2.062	791.900	276.25	6.00
2.292	769.700	275.65	26.00
2.422	757.400	274.85	26.00
2.522	748.000	274.15	23.00
2.622	738.800	273.45	50.00
2.964	707.900	271.65	41.00
3.261	681.900	270.15	42.00
3.444	666.300	270.65	40.00
3.558	656.900	271.85	7.00
4.094	613.900	269.55	11.00
4.569	577.800	266.75	18.00
5.149	536.200	262.45	32.00
5.286	526.700	262.05	26.00
5.653	502.000	259.75	21.00